Integrated RF Interference Suppression Filter Design Using Bond-Wire Inductors

Himanshu Khatri, *Student Member, IEEE*, Prasad S. Gudem, *Member, IEEE*, and Lawrence E. Larson, *Fellow, IEEE*

***Abstract*—Design techniques are presented for the realization of high-performance integrated interference suppression filters using bond-wire inductors. A new configuration is proposed for mitigating the impact of mutual coupling between the bond wires. A differential low-noise amplifier with an integrated on-chip passive interference suppression filter is designed at 2.1 GHz in a 0.18-μm CMOS process, and achieves a transmit leakage suppression of 10 dB at 190-MHz offset. The differential filter uses metal–insulator–metal capacitors and bond-wire inductors and occupies only 0.22 mm^2. The cascaded system achieves a measured gain of 9.5 dB with a 1.6-dB noise figure and −5 dBm out-of-band IIP$_3$ and consumes 11 mA from a 2-V supply.**

***Index Terms*—Bandpass filter (BPF), bond wires, CMOS, interference suppression, mutual inductance, wideband code division multiple access (WCDMA).**

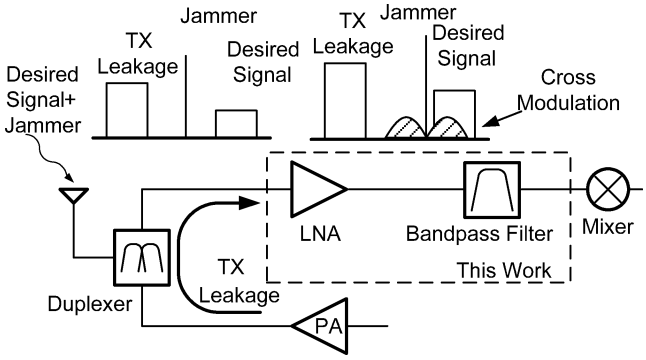

Fig. 1. Cross-modulation (XM) in WCDMA systems [1].

I. Introduction

In MOST frequency-division duplexed (FDD) wireless communication systems, like code division multiple access (CDMA) and wideband code division multiple access (WCDMA), the antenna is shared between the receiver and the transmitter through a duplexer filter. Despite the isolation provided by the duplexer, the transmitted signal appears as the strongest jammer in the receiver and creates cross-modulation distortion (XMD), which degrades the performance of the overall receiver. This often necessitates the use of an interstage RF filter, after the low-noise amplifier (LNA), as shown in Fig. 1 [1]. Such a situation may also arise in multiband receivers, with the transmitter of one band interfering with all the receivers.

Traditionally, on-board ceramic filters were the mainstay for RF filters in this application. Subsequently, they were replaced by surface acoustic wave (SAW) filters, which occupy a lower volume [2]. Recently, thin film bulk acoustic resonator (FBAR) filters have gained much attention due to their smaller form factors, better power-handling capabilities, and temperature insensitivity. They provide excellent performance; e.g., filters centered at several gigahertz having less than 1% fractional bandwidth can be easily constructed with an insertion loss of approximately 3 dB and very high rolloff [3]. Owing to this, the SAW and FBAR filters are extensively used as duplexers and band-select filters. However, these filters are fabricated on piezoelectric materials like $LiNbO_3$ or $LiTaO_3$, which cannot be easily integrated with active circuits. Hence, they are typically packaged separately and occupy additional board area.

In order to overcome this problem, a SAW filter has been successfully stacked on a transceiver chip [4], while an FBAR filter has been integrated at the wafer level [5]. Nevertheless, apart from additional matching networks, these integrations require expensive special masks and extra processing steps. A less expensive on-chip solution is desired.

Unlike the duplexers or other high-selectivity filters, the interstage filters for cellular applications may not require very high rolloff. Fig. 2 shows the relaxation in a typical receiver's linearity specifications as a function of the interstage bandpass filter (BPF) suppression. For example, a 10-dB reduction in transmitter leakage can reduce the IIP$_3$ requirement by 15 dB. Therefore, with recent advances in LNA and mixer design, overall receiver specifications can still be satisfied with an on-chip filter with modest suppression as compared to an FBAR filter. However, low noise figure and excellent linearity are still required.

Numerous attempts have been made to integrate interstage RF filters. For high-frequency operations, doubly terminated ladder filter topologies are preferred for their low sensitivities to filter elements [6]. At several gigahertz, constructing a narrowband (1% fractional bandwidth) bandpass filter employing active-*RC* or Gm-C blocks is quite challenging, due to the resulting dc power and f_{T} requirements [7]. In addition, the resistors and transistors of the active circuit add noise and nonlinearity to the circuit. A *passive LC* ladder filter is a viable option, as it is not constrained by the dc power or transistor f_{T}.

For narrowband bandpass filters, the inductors and capacitors of the *LC* filter should have a high-Q factor to maintain a

Manuscript received July 10, 2007; revised February 4, 2008. This work was supported by the University of California at San Diego (UCSD) Center for Wireless Communications (CWC) and under a University of California (UC) Discovery Grant.

H. Khatri and L. E. Larson are with the Department of Electrical and Computer Engineering, University of California at San Diego, La Jolla, CA 92093 USA (e-mail: hkhatri@ucsd.edu; larson@ece.ucsd.edu).

P. S. Gudem is with Qualcomm Inc., San Diego, CA 92121 USA.

Color versions of one or more of the figures in this paper are available online at http://ieeexplore.ieee.org.

Digital Object Identifier 10.1109/TMTT.2008.921297

0018-9480/$25.00 © 2008 IEEE

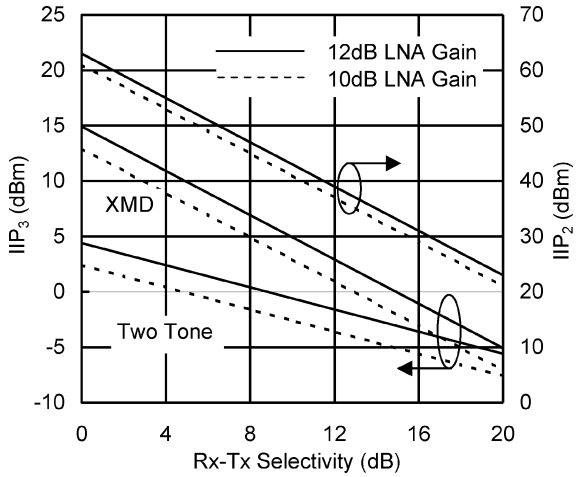

Fig. 2. Variation in required mixer XMD IIP_3, two-tone IIP_3, and IIP_2 against RX–TX suppression of the inter-stage BPF for LNA gains of 12 and 10 dB in a typical WCDMA system.

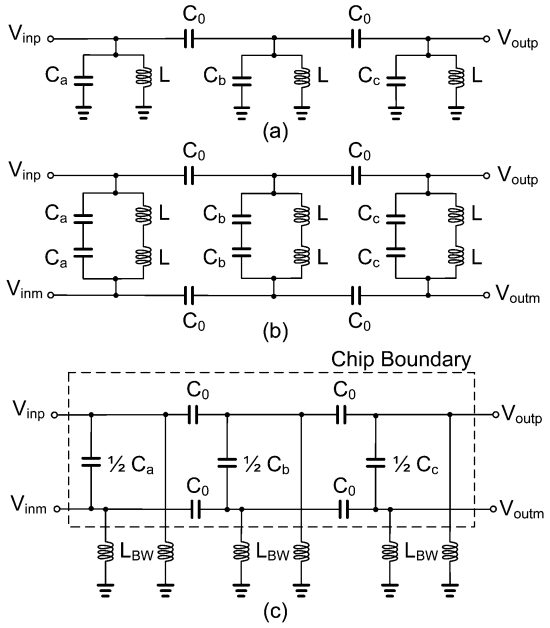

Fig. 3. (a) Single-ended filter. (b) Differential filter. (c) Pseudodifferential filter with equal value bond wires as inductor replacements.

low insertion loss. On-chip metal–insulator–metal (MIM) capacitors with a Q factor of 95 have been reported [8]. However, on-chip spiral inductors suffer from high parasitic resistance and capacitance. Despite this, monolithic *LC* filters have been constructed using Q-enhancement techniques [9]–[15]. All of these implementations occupy a significant area and suffer from poor noise figure ($\geq$ 18 dB) and high nonlinearity (e.g., $P_{1\ \mathrm{dBm}} = -13.4$ dBm with 17.5-mW power consumption at 2.14 GHz [10]).

Hence, there is a need to investigate alternative methods of high-Q inductor implementations, which can be easily integrated and occupy a small die area. One such alternative is the use of bond wires, which are known to be inductive in nature. Typically, the inductance of grounded down bond wires is in the sub-nanohenry range. *LC* ladder filters centered at several gigahertz have similar inductor values, and hence, are amenable for implementation using bond wires. Compared to on-chip spiral inductors, bond wires enjoy high Q factors, and Q factors in excess of 50 have been reported [16], [17].

In this paper, a three-pole differential bandpass filter at 2.14 GHz using bond-wire inductors is presented. Section II gives the topology of a bandpass filter geared toward implementation using on-chip capacitors and bond-wire inductors. Section III summarizes the electrical characteristics of the bond wire and discusses the bond-wire parasitics—resistance and mutual coupling—and their impact on the filter response. The impact of process variations and tuning options are also discussed in Section III. A novel bond-wire configuration is proposed to address the parasitic mutual coupling between the bond wires in Section IV. The LNA/filter combination determines the overall front-end performance. Such a cascaded system for WCDMA is also designed as a proof of concept in Section IV. Subsequent sections discuss the measurement results and discussions.

II. Topology for Bond-Wire-Based Bandpass Filters

An *LC* bandpass ladder filter is typically constructed from low-pass prototypes, whose element values are tabulated in classical texts [18]. The top-C coupled resonator topology shown in Fig. 3(a) has a minimum number of inductors, all terminating to the ground. This structure also has a narrow spread of the component values for high-Q bandpass filters [19]. The topology in Fig. 3(a) offers an opportunity to realize all of the inductors for the filter using equal-valued grounded bond wires. Thus, it removes any need for an on-chip spiral inductor or a bond wire stitched across two pads to realize a series inductor [20]. This has a potential to save tremendous area for on-chip implementations.

However, the practicality of a single-ended implementation of the filter is marred by several factors. The shunt capacitors are terminated to the same ground as the inductors. This is challenging in practice since grounding the capacitors by separate bond wires requires additional bond pads and the resulting $L_{\mathrm{BW}}C$ series combination will alter the capacitor branch susceptance. The filter can still be implemented by scaling the capacitor values [21], but the resulting series resonators create additional attenuation poles. Another solution can be to connect the shunt capacitors together to a common grounded bond wire. This will have an effect of coupling the resonators together, and provide alternate transmission paths creating unintended attenuation poles.

The common package inductance, which connects the package ground plane to the system ground is a nonnegligible fraction of the bond-wire inductance, and can further alter the filter response. Depending on the component values, these parasitics can create attenuation poles, which may appear close to the passband, resulting in serious degradation of the insertion loss.

A differential filter implementation [see Fig. 3(b)] overcomes these problems since there is no need for a common ground node, and the package parasitics appear as common-mode components. Unlike other circuits, where

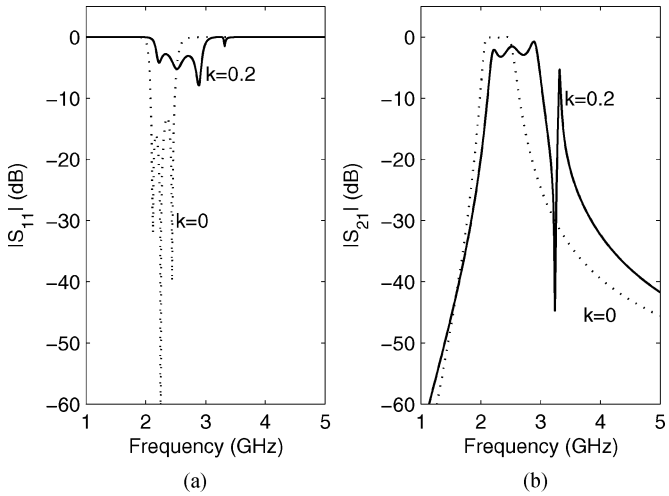

Fig. 4. Simulated: (a) reflection and (b) transmission characteristics of filter with and without mutual inductance.

a differential implementation requires twice the die area of a single-ended version, the on-chip area requirement in this case is approximately halved since the coupling capacitors (C_0) are comparatively smaller than the shunt capacitors ($C_a/C_0 = (1/\sqrt{2}) \cdot (1/\text{fractional bandwidth}) - 1$) for a third-order equiripple filter) and the shunt capacitor values can be halved because of the differential-mode operation. For ease of implementation, it is preferable to terminate the inductors to ground. Hence, a pseudodifferential filter [see Fig. 3(c)] is chosen, where the shunt capacitors are merged together, but the inductors are separately terminated to ground. This configuration will affect the even-mode response of the filter, which will be discussed in Section III.

Bond wires have finite Q factors, which leads to insertion losses in the filter. Apart from parasitic resistance, closely placed bond-wire inductors have nonnegligible mutual inductive coupling. The filter response is significantly altered by the mutual inductances between the bond wires, and this effect must be carefully considered for accurate filter design. Fig. 4 shows one example of this effect: the simulated transmission and input reflection characteristics of a Butterworth third-order filter in the presence and absence of mutual inductance. For the sake of simplicity, a constant coefficient of mutual inductance (k) is assumed and higher order mutual inductances are ignored. In this case, the mutual inductance results in frequency translation, an increased passband ripple, and a new finite attenuation pole. An explanation of this result is provided in Section III.

III. Design Considerations for Bond-Wire-Based Bandpass Filter

A. Bond-Wire Characteristics

An accurate model of the electrical characteristics of the bond wires is crucial for their successful use in a high-performance filter application. In addition to the cross-section radius and material, the electrical properties of bond wires depend on their physical dimensions—their height above the die plane (H), horizontal length (D), and their distance between adjacent bond wires, i.e., their pitch (P). Using the JEDEC-4 point

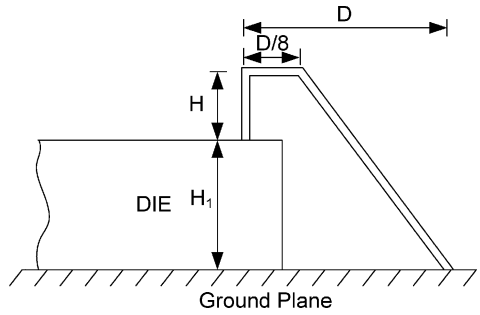

Fig. 5. JEDEC four-point bond-wire model [22].

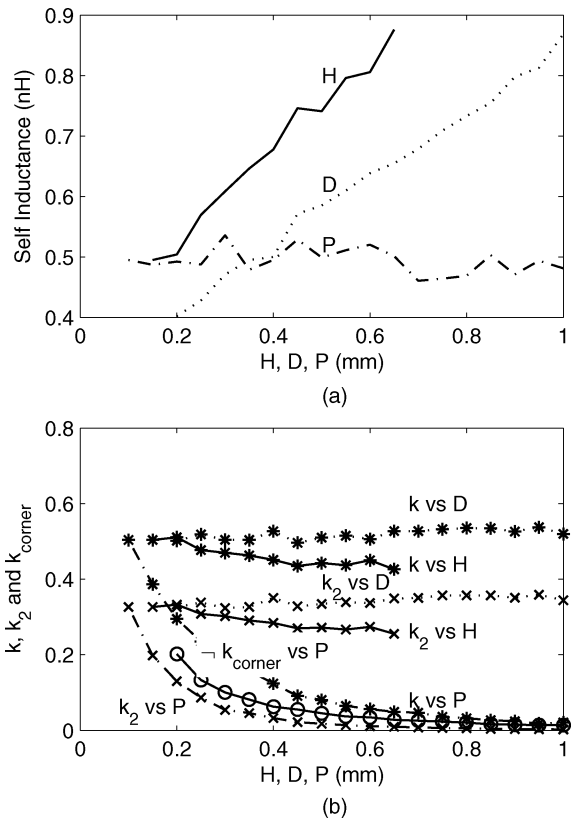

Fig. 6. (a) Simulated variation in bond-wire self-inductance with horizontal length D, height H, and pitch P (b) Simulated variation in coefficient of mutual inductance with adjacent bond wire (k), coefficient of mutual inductance with next to adjacent bond wire (k_2), and coefficient of mutual inductance between bond wires placed along perpendicular edges (k_{corner}) versus H, D, and P. Default H, D, and P values are 150, 350, and 100 μm, respectively.

model for the bond wires (Fig. 5), the total wire length can be geometrically calculated from the horizontal distance (D), the height above the die plane (H), and the die thickness (H_1) [22]. 3-D Ansoft Corporation High Frequency Structure Simulator (HFSS) simulations were performed to study these variations. Fig. 6 shows the simulated variation in the bond-wire self-inductance, the coefficient of mutual inductance between adjacent bond wires (k), and the coefficient of mutual inductance between next-to-adjacent bond wires (k_2). The self-inductance varies linearly with H and D, whereas k and k_2 do not vary significantly with H and D. With increasing pitch (P), the self-inductance remains constant, whereas k and k_2 decay rapidly. Fig. 6(b) also shows the simulated k_{corner} versus P,

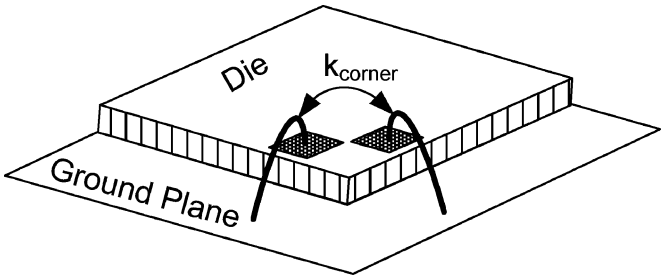

Fig. 7. Orthogonal bond wires at a chip edge.

which is the coefficient of mutual inductance between two bond wires placed along adjacent edges of the die (Fig. 7). Here, the pitch (P) is defined as the distance between the bond wires measured along the edges. This demonstrates that mutual coupling is significantly lowered if bond wires are placed along perpendicular edges.

For a typical die of height 280 μm, a down bond with a height (H) of approximately 150 μm and horizontal distance (D) of 400 μm has a total wire length of roughly 780 μm. This corresponds to a self-inductance of approximately 0.7 nH. For closely placed bond wires with a pitch of 100 μm, the coefficient of mutual inductance (k) is approximately 0.5. Since the coefficient of mutual inductances depends primarily on the bond-wire pitch, it can be approximately controlled by the bond pad placement, and similar coupling can be assumed between uniformly spaced parallel bond wires. The simulations also predict a Q factor of higher than 50 for the bond wires, which is much more than that of a typical on-chip spiral inductor.

However, it is difficult to target a bond wire for a very specific inductance so filters with bond wires having different heights and lengths can be designed for testing purposes, and once an optimal filter performance is achieved, the bond wires can be precisely reproduced by automatic die attach equipment [23].

B. Analysis of Filter Passband Insertion Loss

For a third-order Butterworth filter, $L_{\text{prototype}} = 2$. The insertion loss can be derived for a $2n+1$ section top-C coupled filter as

$$\frac{P_t}{P_{\text{av}}} \approx \left[1 - \frac{R_s}{\omega_0 L_{\text{BW}} Q}\right]^{n+1} \prod_{i=1}^{n} \left[1 - \frac{L_{\text{prototype},2i}}{Q\left(\frac{\omega_c}{\omega_0}\right)}\right] \quad (1)$$

where P_t and P_{av} are the transmitted power and available power of the filter, respectively, R_s is the source resistance, ω_0 is the center frequency, and Q is the quality factor. $L_{\text{prototype},m}$ is the inductor value in the normalized low-pass prototype for the mth section [19]. Fig. 8 shows the simulated and calculated insertion losses of a three-pole filter designed with 0.5-nH inductors centered at 2.14 GHz. For higher Q factors, the calculated loss closely follows the simulated losses, but overestimates it at a lower Q when the source impedance (R_s) becomes comparable to the shunt resistance of the lossy resonators.

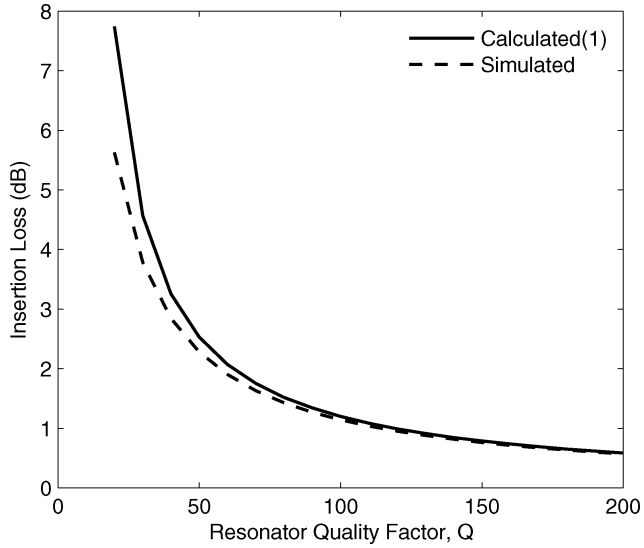

Fig. 8. Simulated versus calculated [using (1)] insertion loss for third-order filter as a function of resonator Q.

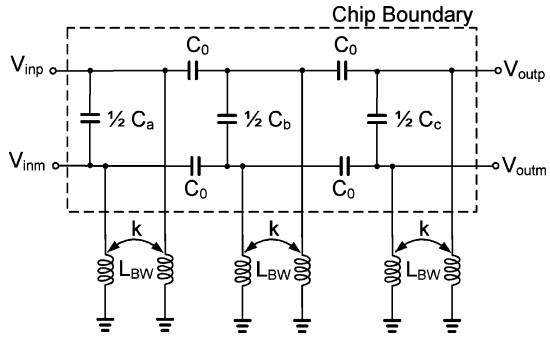

Fig. 9. Differential filter with mutual inductance within the resonator.

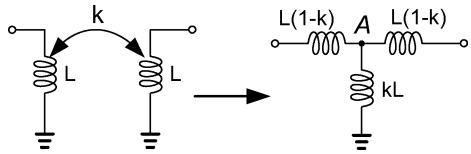

Fig. 10. Equivalent schematic representation of a pair of coupled inductors.

C. Analysis of Mutual Coupling Effect on Filter Response

The effect of mutual inductance on the filter response can be understood by separately examining the effect of mutual coupling *within* a resonator, and *between* resonators.

1) Effect of Mutual Coupling Within Resonators: Consider the mutual inductances between inductors within the same resonators, as shown in Fig. 9. This effect can be equivalently modeled as a T-network of inductors (Fig. 10) [18]. In the differential mode, node *A* is a virtual ground and, thus, the effective self-inductance of either inductor is reduced from L to $L(1-k)$. Hence, the new center frequency is given by

$$\omega_{\text{new}} = \frac{\omega_0}{\sqrt{1-k}}. \quad (2)$$

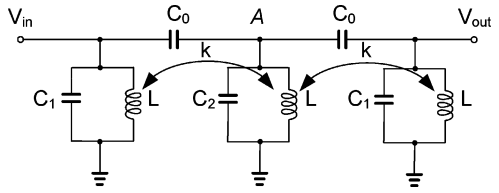

Fig. 11. Ideal single-ended filter with mutual inductance between resonators.

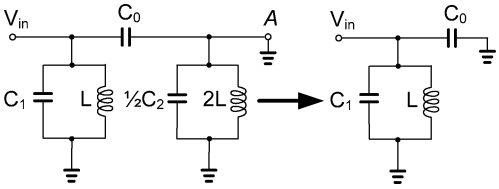

Fig. 12. Odd-mode half-circuit of the single-ended filter.

The effect of the common-mode inductance kL on the circuit response will be considered later.

2) Effect of Mutual Coupling Between Adjacent Resonators: In order to examine some trends, a three-pole single-ended filter (Fig. 11) is analyzed under the following simplifying assumptions.

- The filter is designed for equal source and load terminations so $C_1 = C_3$.
- The resulting filter is tested with an infinite load impedance and it is driven by an ideal current source. The load and source impedances affect the natural frequencies of the filter, but in this case, the Q factors of the attenuation zeros are sufficiently high so that the effect is negligible.
- Only nearest neighbor mutual inductances are considered. For clarity, we first derive the attenuation zeros without any mutual inductance between resonators, and then examine the change in frequency when mutual inductance is present. The analysis is performed using a mode-splitting technique [24], where the circuit resonates at frequencies of the natural response of the system, which are also the attenuation zeros. Moreover, certain frequencies of the natural response can be selectively excited by appropriate choice of the initial excitement: either odd or even mode.

Odd-Mode Analysis Without Mutual Inductance: In this case, equal and opposite current sources are placed at the input and output of the filter in Fig. 11. The center node *A* will, therefore, appear as a virtual ground, and the filter can be reduced to Fig. 12. The resonant frequency is given by

$$\omega_1 = \frac{1}{\sqrt{L(C_1 + C_0)}}. \tag{3}$$

Even-Mode Analysis Without Mutual Inductance: Another mutually exclusive manner to excite the system is to place equal current sources at the input and output. In this scenario, the filter can be drawn as shown in Fig. 13(a), and by symmetry, no current flows through the center node *A*, and it appears as an open node. The filter can then be reduced to a half-circuit, as shown

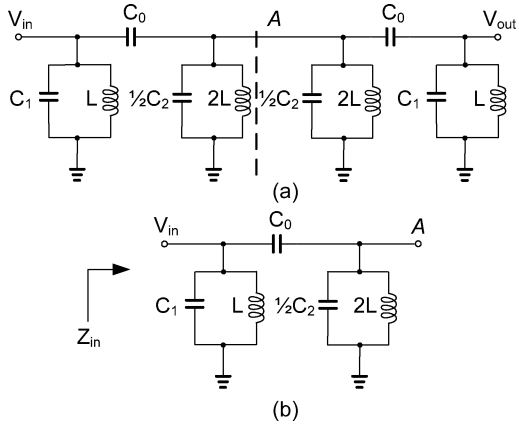

Fig. 13. (a) Symmetric splitting of the single-ended filter. (b) Even-mode half-circuit.

in Fig. 13(b). For this system, the attenuation *zeros* are the *poles* of the input impedance Z_{in} [25]. Z_{in} can be expressed as

$$Z_{\text{in}} = \frac{sL(1 + s^2L(C_2 + 2C_0))}{1 + s^2L(C_1 + C_2 + 3C_0) + s^4L^2(C_1C_2 + (2C_1 + C_2)C_0)}. \tag{4}$$

Thus, the attenuation zeros—or frequencies of natural response of the filter without mutual inductance—are given by

$$\omega_2 = \sqrt{\frac{(C_1 + C_2 + 3C_0) - \sqrt{(C_0 + C_2 - C_1)^2 + 8C_0^2}}{2L(C_1C_2 + (2C_1 + C_2)C_0)}} \tag{5a}$$

$$\omega_3 = \sqrt{\frac{(C_1 + C_2 + 3C_0) + \sqrt{(C_0 + C_2 - C_1)^2 + 8C_0^2}}{2L(C_1C_2 + (2C_1 + C_2)C_0)}}. \tag{5b}$$

For $C_1 = C_2$, this reduces to

$$\omega_2 = \frac{1}{\sqrt{LC_1}} \tag{6a}$$

$$\omega_3 = \frac{1}{\sqrt{L(C_1 + 3C_0)}} \tag{6b}$$

which indicates the coupling effects of the capacitor C_0. These three results (ω_1, ω_2, and ω_3) are the approximate natural frequencies of the filter *without* the effect of coupling between the inductors. We will now examine the effects of mutual coupling between the inductors on the resulting natural frequencies.

Odd-Mode Analysis With Mutual Inductance: As in the case without mutual inductance, the odd-mode excitation renders the center node *A* as a virtual ground and the system again reduces to the circuit of Fig. 12. The resonant frequency is given by

$$\omega_{\mu 1} = \frac{1}{\sqrt{L(C_1 + C_0)}}. \tag{7}$$

Thus, there is no change in the natural frequency in the odd-mode case in the presence of coupling.

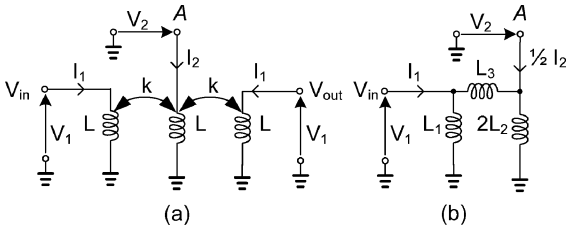

Fig. 14. (a) Even-mode analysis of single-ended coupled filters with mutual inductance. (b) Equivalent even-mode half-circuit.

Even-Mode Analysis With Mutual Inductance: For the case of even-mode excitation, the filter needs to be symmetrically divided into two halves. Consider the network of inductors alone (without C_0, C_1, and C_2), as shown in Fig. 14(a). With even-mode excitation, the V_1 nodes will have equal current. Therefore, the equivalent even-mode half-circuit is in the form of Fig. 14(b).

Writing the Kirchoff's voltage law (KVL) for the circuit in Fig. 14(a),

$$V_1 = sLI_1 + skLI_2 \tag{8a}$$
$$V_2 = 2skLI_1 + sLI_2. \tag{8b}$$

Similarly, for Fig. 14(b),

$$V_1 = s\left(\frac{L_1(L_3+2L_2)}{L_1+2L_2+L_3}\right)I_1 + s\left(\frac{L_1L_2}{L_1+2L_2+L_3}\right)I_2 \tag{9a}$$
$$V_2 = s\left(\frac{2L_1L_2}{L_1+2L_2+L_3}\right)I_1 + s\left(\frac{(L_1+L_3)L_2}{L_1+2L_2+L_3}\right)I_2. \tag{9b}$$

Comparing (8a) and (8b) with (9a) and (9b), respectively, and solving yields

$$L_1 = \frac{1-2k^2}{1-k}L \tag{10a}$$
$$L_2 = \frac{1-2k^2}{1-2k}L \tag{10b}$$
$$L_3 = \frac{1-2k^2}{k}L. \tag{10c}$$

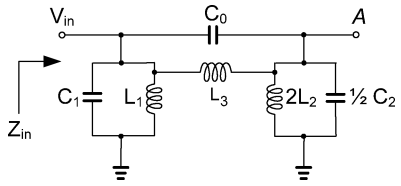

Fig. 15. Equivalent even-mode half-circuit of the filter with mutual coupling between the sections.

Using the inductor model of Fig. 14, the circuit in Fig. 11 can be split into an even-mode half-circuit, as shown in Fig. 15. The attenuation zeros can be computed from the poles of the input impedance Z_{in}, shown in (11) at the bottom of this page. The denominator of (11) is quadratic in s^2, and the corresponding attenuation zero locations are given by (12a) and (12b), shown at the bottom of this page. The preceding analysis suggests that the effect of coupling between the bond wires *within* a resonator results in an upward frequency translation, which can be addressed by designing the filter for a slightly lower center frequency. However, the coupling *between* resonators causes the attenuation zeros to move together, and (as the coupling grows) then separate, as shown in Fig. 16. Fig. 17 depicts the zero movements on the complex s-plane. This pole-splitting has a detrimental effect on the filter performance since it results in increased passband ripple and insertion loss. This mutual coupling can be reduced by placing the bond wires further apart, inserting a grounded shielding bond wire on the chip, or bonding the wires along perpendicular chip edges. Based on these observations, an improved bond-wire configuration is proposed in Section IV.

3) Additional Attenuation Poles and Zeros Due to Mutual Coupling: In the above analysis, the inductive coupling within the resonators and between the resonators was considered separately. When all the inductors are coupled to each other, additional parallel transmission paths are created. In this case, there are two additional paths through mutual inductive coupling—from the input to the center node and from input to the output node. Since the direct coupling is capacitive and the bond-wire coupled paths are inductive, the mutual coupling creates two poles of attenuation when the transmission along

$$Z_{\text{in}} = \frac{\left[sL\left(1+(1-2k^2)s^2L(C_2+2C_0)\right)\right]}{\left[(1+s^2L\left(C_1+C_2+(3-4k)C_0\right)+s^4(1-2k^2)L^2\left(C_1C_2+(2C_1+C_2)C_0\right)\right]} \tag{11}$$

$$\omega_{\mu 2} = \sqrt{\frac{C_1+C_2+(3-4k)C_0-\sqrt{\left(C_1+C_2+(3-4k)C_0\right)^2-4(1-2k^2)\left(C_1C_2+(2C_1+C_2)C_0\right)}}{2(1-2k^2)L\left(C_1C_2+(2C_1+C_2)C_0\right)}} \tag{12a}$$

$$\omega_{\mu 3} = \sqrt{\frac{C_1+C_2+(3-4k)C_0+\sqrt{\left(C_1+C_2+(3-4k)C_0\right)^2-4(1-2k^2)\left(C_1C_2+(2C_1+C_2)C_0\right)}}{2(1-2k^2)L\left(C_1C_2+(2C_1+C_2)C_0\right)}} \tag{12b}$$

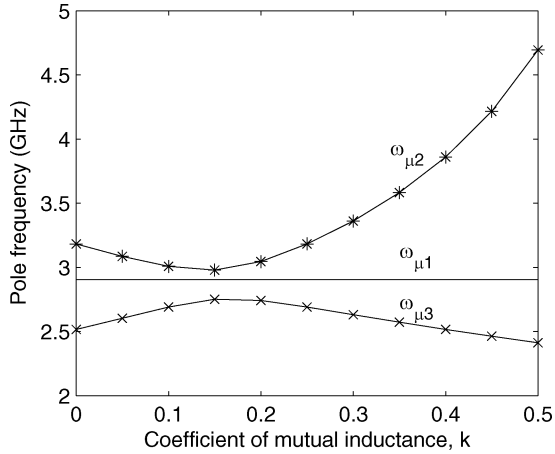

Fig. 16. Variation in attenuation zeros with coefficient of mutual inductance for the filter centered at 2.14 GHz with $L_{\rm BW} = 0.5$ nH. $\omega_{\mu 1}$, $\omega_{\mu 2}$, and $\omega_{\mu 3}$ are given by (7), (12a), and (12b), respectively.

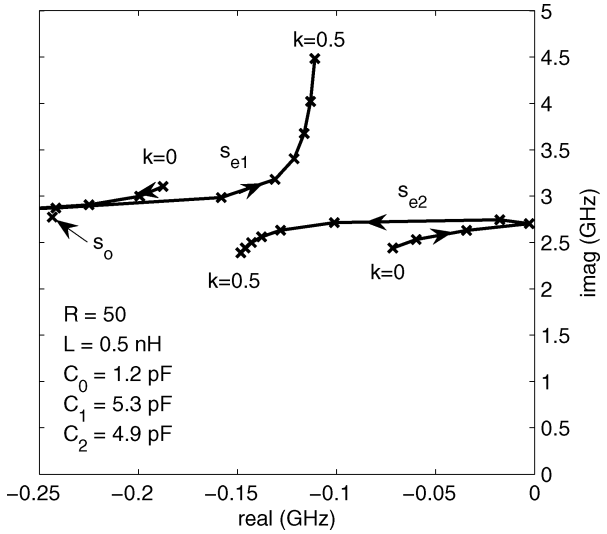

Fig. 17. Pole positions in the complex s-plane with variation in the coefficient of mutual inductance for a filter centered at 2.14 GHz with $L_{\rm BW} = 0.5$ nH. s_o is the odd-mode pole, whereas s_{e1} and s_{e2} are the even-mode poles. Only the dominant poles in $+y$ half-plane are shown.

the parallel paths (through the inductor and capacitor) are equal in magnitude and opposite in phase. One of these poles is seen in Fig. 4.

It is evident from Fig. 6 that there is coupling between next-to-adjacent bond wires as well. These couplings create additional transmission channels and attenuation poles.

D. Analysis of Common-Mode Filter Response

We will first analyze the filter common-mode response when no mutual coupling is present. In the common-mode configuration, there is no current through the shunt capacitors in Fig. 3(b), hence the filter becomes high pass. Using the previously described mode-splitting analysis, it can be found that the attenuation zeros are located at

$$\omega_{\rm cm\,1} = \frac{1}{\sqrt{LC_0}} \tag{13a}$$

$$\omega_{\rm cm\,2} = \frac{1}{\sqrt{3LC_0}}. \tag{13b}$$

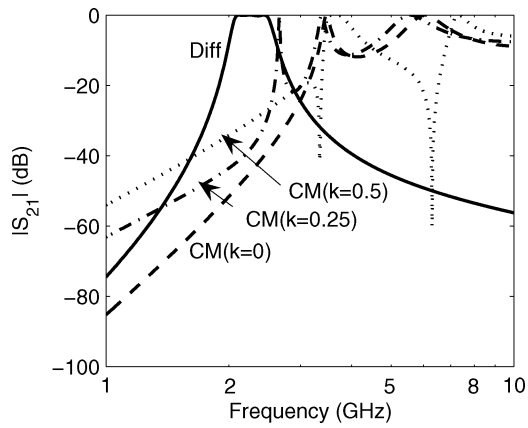

Fig. 18. Differential-mode ($k = 0$) response and common-mode responses for $k = 0$, $k = 0.25$, and $k = 0.5$.

Since C_0 is typically much smaller than C_1, these attenuation zeros are located at higher frequencies than the differential filter passband. The resulting circuit is a five-element filter with a rolloff of 100 dB/decade, hence, the common-mode rejection ratio (CMRR) can be approximately computed as

$$\text{CMRR} \approx 50 \log_{10} \left[\frac{1}{3} \left(1 + \frac{C_1}{C_0} \right) \right]. \tag{14}$$

The common-mode configuration with mutual inductance lacks an equivalent line of symmetry, thus, the mode-splitting technique cannot be used. Intuitively, the mutual inductive coupling creates additional transmission paths, which cancel the signal though the direct path, resulting in loss poles. Fig. 18 shows the simulated differential response along with the common-mode response for different coefficients of mutual inductance. This shows that the mutual inductances further degrade the CMRR response.

E. Process Variations

Any variation in on-chip capacitances or bond-wire inductances can alter the filter response. The capacitances change due to the process and temperature variations, whereas the bond-wire variations are attributed to the inaccuracies in the bonding machine. The modern precision automated bonding machines can reliably reproduce the bonding with an error of less than 5 μm in the dimensions. Hence, once a bond-wire configuration is optimized for the desired filter response through experiments, the variation is less than 5% as the bond-wire dimensions are of the order of 100 μm.

Simulations are conducted on the process corners along with 5% variation in the inductance and Q factor of the bond wires. The filter S_{21} responses for different corners are shown in Fig. 19. The three separated groups of curves corresponds to the FAST, NOM, and SLOW process corners. Typically, the FAST and SLOW corners correspond to $\pm 15\%$ variation from the NOM capacitance. The curves within a group are due to the variations in the bond-wire elements. Hence, capacitance process variations are the primary contributor to the frequency translation. The effect on filter Q is negligible. Simulations reveal that the variations in mutual coupling between the inductors have

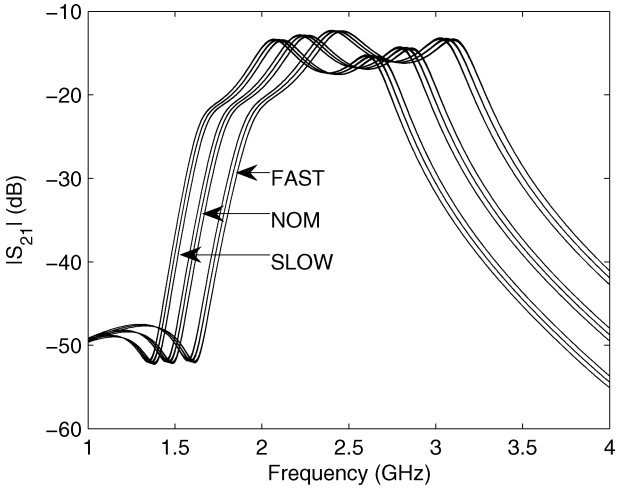

Fig. 19. Corner simulation of the filter S_{21} with process corners and 5% variation in bond-wire inductance and quality factor.

some impact on the filter Q and bandwidth. However, they have negligible effect on the filter rolloff at the lower stopband where the transmitter signal lies.

F. Filter Tuning

The variations in the filter response necessitates a tunable filter. Metal–oxide–semiconductor (MOS) capacitors and p-n junctions are typically used as varactors for the tuning purposes. For tuning integrated circuits, MOS varactors are generally preferred for their broader tuning range ($\pm 30\%$) as compared to the p-n junction varactors ($\pm 20\%$) over the same tuning voltage range [26]. However, the MOS varactors are nonlinear in the tuning range and the minimum Q factor of the MOS varactors is around 20–30 [25]–[29]. This may be acceptable in designs involving on-chip spiral inductors with lower Q factors, but can be a significant contributor to the insertion losses in the filter under consideration.

As discussed in Section III-E, the variation in the bond wires is much smaller than that of the on-chip capacitors. Hence, $\pm 20\%$ tuning range of the p-n junction varactor should suffice for tuning this filter. The p-n junction varactors usually have a better quality factor than the MOS varactors. These varactors can also be configured to achieve very high linearity [30]. Another approach can be using a parallel bank of MOS varactors, each varactor being biased either at high or low voltage. In these operating regions, the MOS varactors have a high-Q factor and linearity [31].

IV. WCDMA CMOS LNA and Bandpass Filter Design

As the mutual coupling analysis demonstrated, the input and output resonator sections should be isolated from each other to prevent finite attenuation poles being created around the passband. This can be accomplished by placing grounded bond wires between the sections or by placing the corresponding bond wires along perpendicular sections, as shown in Fig. 7. The latter method was preferred since it occupies less die area. In the proposed configuration, these bond wires of the central resonator were placed in between the two bond wires of the input resonator, as shown in Fig. 20, to minimize the differential- to

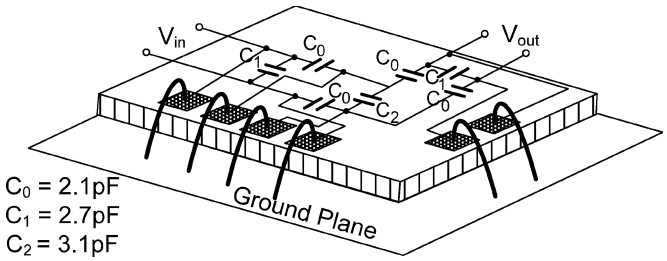

Fig. 20. Proposed bond-wire configuration for on-chip filter.

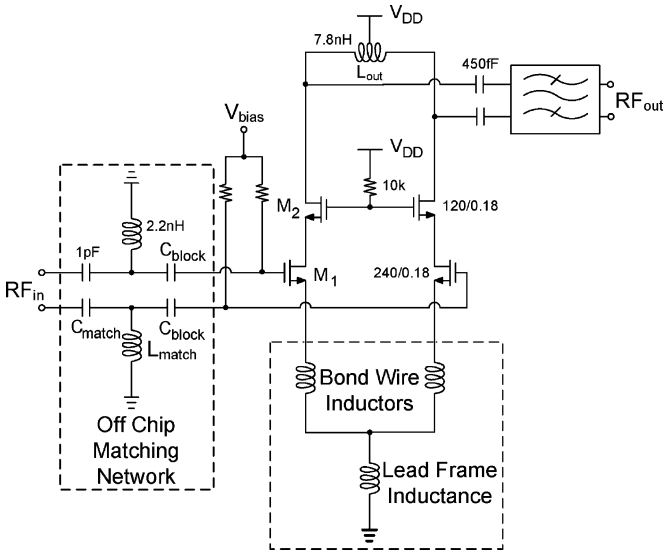

Fig. 21. WCDMA CMOS LNA schematic. The output of the LNA drives the bandpass filter.

common-mode conversion by maintaining a differential symmetry. Full 3-D electromagnetic (EM) simulations were performed for this bond-wire configuration and the results were used in the filter design. The on-chip capacitances were tuned to obtain the best performance with this bond-wire configuration.

The LNA/filter combination determines the overall front-end performance. As shown in Fig. 21, a pseudodifferential cascode topology is chosen for the LNA for improved headroom and isolation, and ease of integration with the differential on-chip bandpass filter of Fig. 20. A bias current of 5.5 mA per branch is chosen to achieve optimum linearity, and the transistor width is optimized for noise performance. The source degeneration is provided by bond wires terminating on a single lead pin, which is connected to ground through the lead frame of the package; the lead pin inductance provides some common-mode rejection.

The cascaded system of the LNA and the bandpass filter is optimized for end-to-end gain and noise performance. The LNA input is matched using an off-chip *LC* section, while the filter is tuned for 100-Ω differential output impedance. The LNA output is matched to the filter input.

V. Measurement Results

A. Bandpass Filter

For testing purposes, the filter was fabricated standalone. It is comprised of 1-fF/μm^2 MIM capacitors and 1.2-mil gold bond

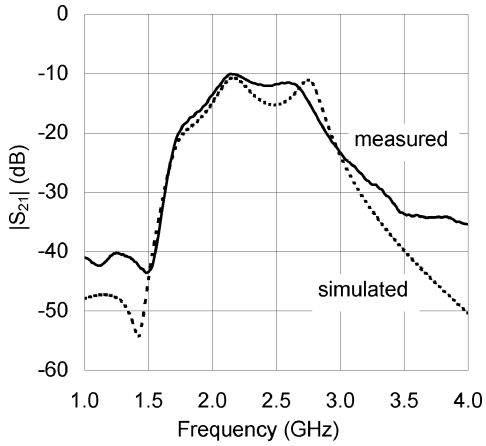

Fig. 22. Measured and simulated S_{21} of the bandpass filter, shown via solid and dashed lines, respectively.

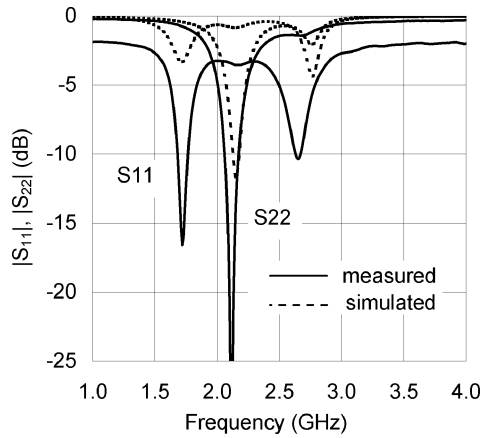

Fig. 23. Measured and simulated S_{11} and S_{22} of the bandpass filter, shown via solid and dashed lines, respectively.

wires. The filter measures 400×550 μm^2 without the input and output bonding pads. The input and output were probed using ground–signal–signal–ground (GSSG) differential probes and stripline 180° hybrids were used for balanced to unbalanced conversion. Fig. 22 shows the measured filter transmission response along with the simulated transmission response with the layout parasitics back-annotated. The transmission zero appearing in the S_{21} plot around 1.5 GHz is attributed to the small residual mutual coupling between the orthogonal bondwire sets. The measured and simulated input and output reflection responses are shown in Fig. 23. The relatively high input reflection coefficient is due to the fact that the filter input is matched to the LNA output impedance, rather than 50 Ω. The slight mismatch between the measured and simulated S_{11} is due to series resistance in the balun and GSSG probes.

B. Cascaded LNA and Bandpass Filter

The cascaded system of the LNA and the filter was fabricated in a 0.18-μm CMOS process. The LNA occupies 390×270 μm^2 without the bonding pads. A microphotograph of the complete system is shown in Fig. 24. The circuit had a gain of 9.5 dB at 2110 MHz and achieved a TX/RX suppression of 10 dB at 1920 MHz (190-MHz offset), as shown in Fig. 25.

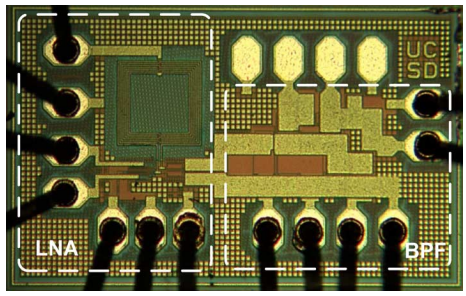

Fig. 24. Microphotograph of the CMOS LNA and BPF. The chip occupies 1025×600 μm^2.

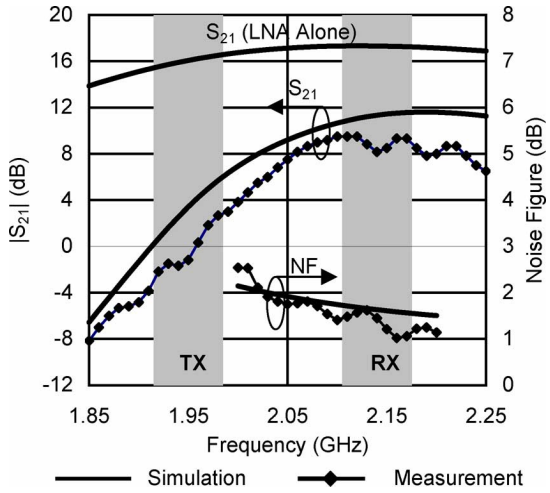

Fig. 25. Measured gain of the LNA and BPF. The TX/RX suppression is 11 dB, and the noise figure is less than 1.6 dB.

TABLE I
MEASUREMENT RESULTS

Specification	Measurement	Simulation	Unit
RX Band	2110-2170	2110-2170	MHz
TX Band	1920-1980	1920-1980	MHz
Gain (Rx)	9.5	11.4	dB
Noise Figure	$\leq$ 1.6	1.45	dB
Tx Rejection	10	9	dB
IIP_3 (cross-modulation)	-5	-4	dBm
IIP_3 (out-of-band)	-5	-3	dBm
IIP_3 (in-band)	-10	-5.5	dBm
S_{11}	-7		dB
S_{22}	-12	$\leq$ -10	dB
Power	11mA @ 2V	11mA @ 2V	

The measured noise figure was less than 1.6 dB in the passband. The input and output return losses were −7 and −12 dB, respectively. For three-tone XM test, two −30-dBm tones were placed at the TX frequency of 1920 MHz ± 1.25 MHz and the third jammer tone with −45-dBm power was placed at 2137.5 MHz. The resultant XM distortion was measured at 2140 MHz and the corresponding XM IIP_3 was −5 dBm. The out-of-band linearity test was conducted with two tones at 1950 and 2045 MHz and the resulting IIP_3 was −5 dBm. The in-band IIP_3 measurement was conducted with 10 MHz and 20-MHz offset tones and was found to be −10 dBm. The input 1-dB gain compression point at 2140 MHz was −20 dBm. The results are summarized in Table I. The agreement between

simulated and measured results is excellent, demonstrating the efficacy of the filter design approach described above.

VI. Conclusion

The challenge of on-chip bandpass filter design presents a perennial problem to the wireless system designer. The use of grounded bond wires as a resonator technology is an attractive alternative to more traditional approaches. The advantage of the lower loss that these devices possess must be balanced against their limited range of values and high degree of mutual coupling.

This paper has highlighted some potential solutions to these limitations, and we presented design techniques to mitigate some of the problems. A WCDMA CMOS LNA with a bond-wire-based integrated transmit interference suppression filter demonstrated that high performance could be achieved at the expense of slightly higher noise figure, and the extra area required for the filter itself. These promising approaches point the way toward expanded use of these techniques in the future.

Acknowledgment

The authors would like to acknowledge valuable discussions with Prof. G. Rebeiz and Prof. P. Asbeck, both with the University of California at San Diego (UCSD), Prof. D. Lie, Texas Tech. University, Lubboch, and D. Kimball, California Institute of Telecommunications and Information Technology, UCSD. The authors would also like to acknowledge the valuable support of Jazz Semiconductor, Newport Beach, CA, for integrated circuit fabrication and J. Cordovez, Jazz Semiconductor, for fabrication support. The authors acknowledge the support of the UCSD Center for Wireless Communications and its Member Companies.

References

[1] V. Aparin and L. Larson, "Analysis and reduction of cross-modulation distortion in CDMA receivers," *IEEE Trans. Microw. Theory Tech.*, vol. 51, no. 5, pp. 1591–1602, May 2003.

[2] R. Ruby, P. Bradley, J. Larson, III, Y. Oshmyansky, and D. Figueredo, "Ultra-miniature high-Q filters and duplexers using FBAR technology," in *IEEE ISSCC Tech. Dig.*, 2001, pp. 120–121.

[3] R. Weigel, D. Morgan, J. Owens, A. Ballato, K. Lakin, K. Hashimoto, and C. Ruppel, "Microwave acoustic materials, devices, and applications," *IEEE Trans. Microw. Theory Tech.*, vol. 50, no. 3, pp. 738–749, Mar. 2002.

[4] R. Jones *et al.*, "System-in-a-package integration of SAW RF RX filter stacked on a transceiver chip," *IEEE Trans. Adv. Packag.*, vol. 28, no. 2, pp. 310–319, Feb. 2005.

[5] M. Dubois, C. Billard, C. Muller, G. Parat, and P. Vincent, "Integration of high-Q BAW resonators and filters above IC," in *IEEE ISSCC Tech. Dig.*, 2005, pp. 392–394.

[6] R. Schaumann and M. Van Valkenburg, *Design of Analog Filters*. Oxford, U.K.: Oxford Univ. Press, 2001, ch. 13.

[7] Y. Tsividis, "Continuous-time filters in telecommunications chips," *IEEE Commun. Mag.*, vol. 39, no. 4, pp. 132–137, Apr. 2001.

[8] R. Aparicio and A. Hajimiri, "Capacity limits and matching properties of integrated capacitors," *IEEE J. Solid-State Circuits*, vol. 37, no. 3, pp. 384–393, Mar. 2002.

[9] D. Li and Y. Tsividis, "A 1.9 GHz Si active *LC* filter with on-chip automatic tuning," in *IEEE ISSCC Tech. Dig.*, 2001, pp. 368–369.

[10] T. Soorapanth and S. S. Wong, "A 0-dB IL 2140 $\pm$ 30 MHz bandpass filter utilizing Q-enhanced spiral inductors in standard CMOS," *IEEE J. Solid-State Circuits*, vol. 37, no. 5, pp. 579–586, May 2002.

[11] W. Kuhn, F. Stephenson, and A. Elshabini-Riad, "Dynamic range of high-Q OTA-C and enhanced-Q *LC* RF bandpass filters," in *Proc. 37th Midwest Circuits Syst. Symp.*, 1994, pp. 767–771.

[12] R. Duncan, K. Martin, and A. Sedra, "A Q-enhanced active-*RLC* filter," *IEEE Trans. Circuits Syst. II, Analog, Digit. Signal Process.*, vol. 44, no. 5, pp. 341–347, May 1997.

[13] F. Dulger, E. Sanchez-Sinencio, and J. Silva-Martinez, "A 1.3-V 5-mW fully integrated tunable bandpass filter at 2.1 GHz in 0.35-μm CMOS," *IEEE J. Solid-State Circuits*, vol. 38, no. 6, pp. 918–928, Jun. 2003.

[14] A. Mohieldin, E. Sanchez-Sinencio, and J. Silva-Martinez, "A 2.7-V 1.8-GHz fourth-order tunable *LC* bandpass filter based on emulation of magnetically coupled resonators," *IEEE J. Solid-State Circuits*, vol. 38, no. 7, pp. 1172–1181, Jul. 2003.

[15] S. Li, S. Sengupta, H. Dinc, and P. Allen, "CMOS high-linear wide-dynamic range RF on-chip filters using Q-enhanced *LC* filters," in *IEEE Int. Circuits Syst. Symp.*, 2005, pp. 5942–5945.

[16] A. Dec and K. Suyama, "A 1.9-GHz CMOS VCO with micromachined elecromechanically tunable capacitors," *IEEE J. Solid-State Circuits*, vol. 35, no. 8, pp. 1231–1237, Aug. 2000.

[17] A. Dec and K. Suyama, "Microwave MEMS-based voltage-controlled oscillators," *IEEE Trans. Microw. Theory Tech.*, vol. 48, no. 11, pp. 1943–1949, Nov. 2000.

[18] A. I. Zverev, *Handbook of Filter Synthesis*. New York: Wiley, 1967.

[19] J. B. Hagen, *Radio-Frequency Electronics*. Cambridge, U.K.: Cambridge Univ. Press, 1996.

[20] J. Craninckx and M. Steyaert, "A 1.8-GHz CMOS low-phase-noise voltage-controlled oscillator with prescaler," *IEEE J. Solid-State Circuits*, vol. 30, no. 12, pp. 1474–1482, Dec. 1995.

[21] H. Khatri, L. Larson, and D. Lie, "On-chip monolithic filters for receiver interference suppression using bond-wire inductors," in *SiRF Dig.*, 2006, pp. 166–169.

[22] *Bond Wire Modeling Standard*, EIA/JEDEC Standard EIA/JESD59, Jun. 1997.

[23] T. Ahrens and T. Lee, "A 1.4-GHz 3-mW CMOS *LC* low phase noise VCO using tapped bond wire inductances," in *Proc. Int. Low-Power Electron. Design Symp.*, 1998, pp. 16–19.

[24] T. H. Lee, *Planar Microwave Engineering*. Cambridge, U.K.: Cambridge Univ. Press, 2004.

[25] G. Matthaei, L. Young, and E. M. T. Jones, *Microwave Filter, Impedance-Matching Networks, and Coupling Structures*. Norwood, MA: Artech House, 1980.

[26] F. Svelto, P. Erratico, S. Manzini, and R. Castello, "A metal–oxide–semiconductor varactor," *IEEE Electron Device Lett.*, vol. 20, no. 4, pp. 164–166, Apr. 1999.

[27] A. Porret, T. Melly, C. Enz, and E. Vittoz, "Design of high-Q varactors for low-power wireless applications using a standard CMOS process," *IEEE J. Solid-State Circuits*, vol. 35, no. 3, pp. 337–345, Mar. 2000.

[28] M. Tiebout, "Low-power low-phase-noise differentially tuned quadrature VCO design in standard CMOS," *IEEE J. Solid-State Circuits*, vol. 36, no. 7, pp. 1018–1024, Jul. 2001.

[29] K. Molnar, G. Rappitsch, Z. Huszka, and E. Seebacher, "MOS varactor modeling with a subcircuit utilizing the BSIM3v3 model," *IEEE Trans. Electron Devices*, vol. 49, no. 7, pp. 1206–1211, Jul. 2002.

[30] K. Buisman, L. de Vreede, L. Larson, M. Spirito, A. Akhnoukh, T. Scholtes, and L. Nanver, "Distortion-free varactor diode topologies for RF adaptivity," in *IEEE MTT-S Int. Microw. Symp. Dig.*, 2005, pp. 157–160.

[31] J. Mourant, J. Imbornone, and T. Tewksbury, "A low phase noise monolithic VCO in SiGe BiCMOS," in *IEEE RFIC Symp. Dig.*, 2000, pp. 65–68.

Himanshu Khatri (S'05) received the B.Tech. degree in electrical engineering from the Indian Institute of Technology Kanpur, India, in 2002, the M.S. degree in electrical engineering from the University of California at San Diego (UCSD), La Jolla, in 2005, and is currently working toward the Ph.D. degree at UCSD.

From 2002 to 2003, he was involved with very large scale integration (VLSI) computer-aided design (CAD) tool development with Atrenta India. In 2004, he interned with Qualcomm Inc., San Diego, CA, where he has been involved with mixer design. He is currently and Intern with Qualcomm Inc., where he designs CDMA2000 receiver front-ends. His research concerns interference mitigation techniques in receivers for advanced wireless communication systems

Prasad S. Gudem (M'96) received the B. Tech degree from the Indian Institute of Technology, Madras, India, in 1988, and the Ph.D. degree from the University of Waterloo, Waterloo, ON, Canada, in 1996, both in electrical engineering.

From 1997 to 2000, he was with Cadence Design Systems, San Diego, CA, where he was involved in semiconductor-device modeling for analog and RF applications. In 2000, he joined the IBM Watson Research Center, where he was involved with RF integrated-circuit design for WCDMA applications using IBM's SiGe technology. In 2002, he joined Qualcomm Inc., San Diego, CA, as Staff Engineer and lead the development of diversity receiver for CDMA2000/WCDMA applications. As the Director of Engineering with the Analog/RF Integrated Circuit (IC) Design Group, Qualcomm Inc., he has continued to lead the development of next-generation transceivers for cellular applications. Since 2000, he has taught several graduate-level classes and co-advised several Ph.D. students in the area of RF IC design at the University of California at San Diego, La Jolla.

Dr. Gudem was the recipient of the Graduate Teaching Award for the 2001–2002 academic year in recognition of his outstanding teaching of the ECE265 course sequence "Communication Circuit Design: I, II, and III."

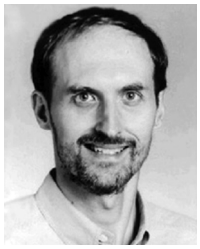

Lawrence E. Larson (S'82–M'86–SM'90–F'00) received the B.S. and M.Eng. degrees in electrical engineering from Cornell University, Ithaca, NY, in 1979 and 1980, respectively, and the Ph.D. degree in electrical engineering and M.B.A. degree from the University of California at Los Angeles (UCLA), in 1986 and 1996, respectively.

From 1980 to 1996, he was with Hughes Research Laboratories, Malibu, CA, where he directed the development of high-frequency microelectronics in GaAs, InP, and Si–SiGe and microelectromechanical systems (MEMS) technologies. In 1996, he joined the faculty of the University of California at San Diego (UCSD), La Jolla, where he is the Inaugural Holder of the Communications Industry Chair. He is currently Director of the UCSD Center for Wireless Communications. During the 2000–2001 academic years, he was on leave with IBM Research, San Diego, CA, where he directed the development of RF integrated circuits (RFICs) for third-generation (3G) applications. During the 2004–2005 academic year, he was a Visiting Professor with the Technical University of Delft, Delft, The Netherlands. He has authored or coauthored over 250 papers. He holds 31 U.S. patents.

Dr. Larson was the recipient of the 1995 Hughes Electronics Sector Patent Award for his research on RF MEMS technology. He was corecipient of the 1996 Lawrence A. Hyland Patent Award of Hughes Electronics for his research on low-noise millimeter-wave HEMTs, the 1999 IBM Microelectronics Excellence Award for his research in Si–SiGe heterojunction bipolar transistor technology, and the 2003 IEEE Custom Integrated Circuits Conference Best Invited Paper Award.